INTERNATIONAL JOURNAL OF HYDROGEN ENERGY 45 (2020) 7488–7496

Available online at www.sciencedirect.com

ScienceDirect

journal homepage: www.elsevier.com/locate/he

Formation of hydrogen bubbles in Pd-Ag membranes during H_2 permeation

T.A. Peters*, P.A. Carvalho, M. Stange, R. Bredesen

SINTEF Industry, P.O. Box 124 Blindern, N-0314, Oslo, Norway

ARTICLE INFO

Article history:
Received 23 November 2018
Received in revised form
25 January 2019
Accepted 2 February 2019
Available online 1 March 2019

Keywords:
Pd-Ag membrane
H_2 bubbles
Pinhole formation
STEM characterisation

ABSTRACT

Palladium membranes used for hydrogen separation seemingly develop cavities filled with hydrogen, *i.e.* hydrogen bubbles, along the grain boundaries. These bubbles may represent initial stages of pinhole formation that lead to unselective leakage and compromise the long-term stability of the membranes. Alloying with Ag improves the permeability of Pd, but whether these H_2 bubbles form in Pd-Ag membranes remained unknown. In this work, the microstructure of a $Pd_{77}Ag_{23}$ membrane was characterized by electron microscopy after H_2 permeation testing for 50 days at 15 bar at temperatures up to 450 °C. The results show that Ag does not prevent bubbles from emerging along high-angle grain boundaries, but reduces the number of potential nucleation sites for cavity formation by supressing the development of dislocation networks when H-saturated Pd is cycled through the miscibility gap. Both magnetron-sputtered and electroless plated membranes are afflicted by H_2 bubbles, thus their formation seems determined by intrinsic properties of the material independent of the fabrication technique. The qualitative discussion enables to point directions for enhancement of membrane stability.

Introduction

Palladium-based membrane technology has unique hydrogen separation capabilities and shows market potential for production of high-purity H_2. Pd-based membranes are therefore regarded as a Key Enabling Technology (KET) to facilitate the transition towards a low carbon and resource-efficient and technology-based H_2 economy [1,2]. The membranes can operate at high transmembrane pressure differences at elevated temperatures, typically 300–500 °C, and are capable of separating hydrogen from gas mixtures containing CO, H_2O, CH_4 and other gases. These conditions represent an excellent match with processes of H_2 production from various feedstocks [3]. Combining these membranes with appropriate catalysts in membrane reactors to produce hydrogen from different sources has been described in numerous studies [4–8]. Such a membrane separation may improve the thermo-chemical performance of the energy system, while reducing the power plant complexity, and potentially its cost [7,9,10]. Tokyo Gas has developed the world's largest scale of membrane reformer with a rated H_2 production capacity of 40 Nm^3/h for on-site hydrogen production from natural gas, achieving the world's highest hydrogen production efficiency of 81.4% [11,12]. A thorough overview of Pd-based membranes in hydrogen production for fuel cells can be found in Refs. [13,14].

Even though membrane stability over periods exceeding 10,000 h is currently achieved [3,11], it is clear that long-term stability under relevant temperature and pressure conditions, especially for integrated reforming [15], is challenging

* *Corresponding author.*
E-mail address: thijs.peters@sintef.no (T.A. Peters).
https://doi.org/10.1016/j.ijhydene.2019.02.001

due to microstructural changes occurring in the thin Pd membrane layer, such as pinhole formation. Pinholes have been proposed to result from 'inhomogeneous sintering' of Pd crystallites [16], but such mechanism can hardly justify changes in membranes with an initial well-consolidated structure [17]. In this case, the pinholes represent an increase of the membrane free surface and cannot result solely from heat treatment which, instead, should bring the metallic system closer to equilibrium by minimization of the surface area. Nonetheless, it is indisputable that prolonged exposure to H_2 at high temperatures promotes pinhole formation in Pd-based membranes [16,18,19]. The phenomenon appears to result from temperature-activated lattice diffusion processes mediated by hydrogen [17], through mechanisms governed by driving forces that remain to be fully elucidated and which may show low saturation threshold in terms of dissolved H [17].

In a previous work, a thorough characterisation of a ceramic-supported 5 micron-thick pure Pd membrane prepared by electroless plating and operated over a period of 100 days at 450 °C and 27 bar with a feed representing steam-methane-reforming conditions was performed [17]. Analysis of the membrane cross-section revealed a high density of cavities that grew to sizes up to tens of nanometers. It was suggested that these defects resulted from coalescence of hydrogen-vacancy complexes ($H_x\square$) at low-energy sites, such as low- and high-angle grain boundaries (GBs), followed by molecular recombination of the hydrogen atoms [17]. In addition, dislocation entanglements generated upon cooling across the Pd-H miscibility gap were rearranged into dislocation walls, *i.e.* low-angle GBs [20]. Based on these findings, it was suggested that the cavities present at the low-angle GBs were formed during shutdown procedures as a result of forced supersaturation (decompression-sickness type of phenomenon [21]), while cavities at high-angle GBs may have nucleated during high temperature operation over time [17].

In the current work, a thorough microstructural characterisation of a $Pd_{77}Ag_{23}$ membrane employed in a porous stainless steel (PSS) supported microchannel module after operation for 50 days at a pressure of up to 15 bar at a temperature of 450 °C is presented. The goal is to investigate the role of hydrogen permeation on the structural changes occurring during high-temperature operation. In addition, it is simultaneously assessed whether alloying with Ag prevents the formation of dislocation entanglements and their rearrangement into low-angle GBs. Alloying is conveniently used to depress the hydride phase miscibility gap below room temperature and simultaneously enhance permeability and lower the material cost [22]. In addition, palladium-silver alloys (Pd-Ag) show higher permeability compared to pure palladium. The hydrogen solubility increases with silver content and reaches a maximum at 20–40% Ag, while the diffusion coefficient shows the opposite behaviour [23–26], resulting in a permeability 1.7 times higher for the $Pd_{77}Ag_{23}$ alloy compared to pure Pd at 350 °C [27,28]. Finally, the aim is to investigate if cavity formation is restricted to specific techniques of membrane fabrication. The pure Pd membrane investigated previously [17] was prepared by electroless plating, the most widely used Pd-based membrane fabrication technique, while the current $Pd_{77}Ag_{23}$ membrane was manufactured by magnetron sputtering, which is able to produce alloy membranes with controlled stoichiometry [29,30]. Influence of the fabrication technique on the long-term stability of palladium-gold (Pd-Au) membranes tested in H_2S-containing atmospheres has been found before [31]. Membranes produced by sputtering experienced irreversible loss of hydrogen selectivity upon sulfur exposure within a day due to significant decrease in membrane thickness, while no equivalent decrease in thickness or selectivity was observed for cold-worked membranes. In addition, cast and rolled foils, which have smoother surfaces, were less prone to surface changes induced by H_2S compared to rougher surface foils, due to lower sulfur adsorption on the former [32].

Experimental

Pd-Ag microchannel module and operation

An unsupported Pd-Ag film was prepared onto a silicon single crystal substrate using a CVC 601 magnetron sputtering apparatus from a single phase $Pd_{77}Ag_{23}$ alloy target as described previously [33–35]. The nominal thickness of the film applied in this study was 10 μm. After sputtering, the $Pd_{77}Ag_{23}$ film was removed manually from the silicon substrate and integrated into the porous stainless steel supported microchannel module. The feed section of the module consists of seven parallel machined channels with dimensions $1 \times 1 \times 13$ mm^3, providing a total of 0.91 cm^2 active membrane area. On the permeate side, a porous stainless steel (PSS) support with a thickness of 3 mm has been employed (SIKA-R1, 1 μm rating supplied GKN Sinter Metals, Germany). In between the feed and permeate section, the free-standing $Pd_{77}Ag_{23}$ film with nominal thickness of 10 μm prepared by magnetron sputtering was fitted. Sealing was obtained by clamping between the two highly-polished parts of the module. More information on the module can be found in Ref. [35]. A schematic representation of the cross-section of the microchannel module is shown in Fig. 1. The configuration of the $Pd_{77}Ag_{23}$ membrane consisted of alternating permeation channels and regions blocked by steel fins on the feed side. The Pd-alloy film area in contact with the fins between the channels was assumed not to take part in permeation.

The performance of the PSS-supported $Pd_{77}Ag_{23}$ membrane was presented in detail elsewhere [35], but for the sake of completeness is concisely summarised below. For this

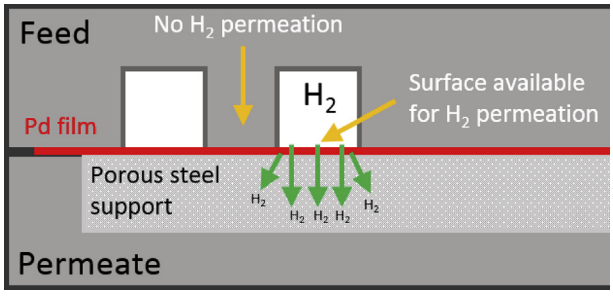

Fig. 1 – Schematic cross-section representation of the porous stainless steel supported microchannel module.

particular microchannel module, a hydrogen flux of 195.3 mL $min^{-1}\cdot cm^{-2}$ is obtained at 450 °C and 5 bars of feed pressure, corresponding to a permeability of 3.4 × 10^{-8} mol m^{-1} $s^{-1}\cdot Pa^{-0.5}$, in agreement with values obtained for tubular Pd–23%Ag/stainless steel composite membranes [36]. Subsequently, the membrane was operated for 50 days at 450 °C, showing high stability up to the highest feed pressure applied of 15 bars, see Fig. 2.

Even though a minor intermetal diffusion between the $Pd_{77}Ag_{23}$ film and the underlying PSS support, and porosity on the membrane surface was found after the operation [35], the N_2 leakage flux remained below the detection limit of the equipment, *i.e.* 5 μL $cm^{-2}\cdot min^{-1}$, resulting in a minimum value for the H_2/N_2 permselectivity of 39,000 applying the pure H_2 flux value obtained at 5 bars. More details on the performance, and an initial post-process macrostructural characterisation of the module can be found in Ref. [35].

Microstructural characterisation

The plan-view and cross-section microstructure of the membrane was characterized after the permeation experiments by scanning electron microscopy (SEM) using secondary electrons (SE) or backscattered electrons (BSE), with an FEI 650 NOVA NanoSEM instrument. Transmission and scanning transmission electron microscopy (S/TEM) of membrane cross-sections was carried out at 300 kV with an FEI Titan G2 60–300 instrument equipped with a DCOR probe Cs-aberration corrector and a Super-X Bruker energy dispersive spectrometer with 4 silicon drift detectors. TEM imaging was carried out in bright field mode coupled to selected area electron diffraction (SAED). High-angle annular dark field (HAADF) imaging was performed with a probe current of ~100 pA and nominal spatial resolution of 0.08 nm. The convergence and collection angles employed are indicated for each STEM image. Lattice images were indexed using fast Fourier transforms (FFT) and strain was evaluated by geometric phase analysis (GPA) using the FRWRtools plugin [37] implemented in Digital Micrograph (Gatan Inc). The samples were prepared by focused ion beam (Ga^+) with a JEOL JIB 4500 Multibeam instrument.

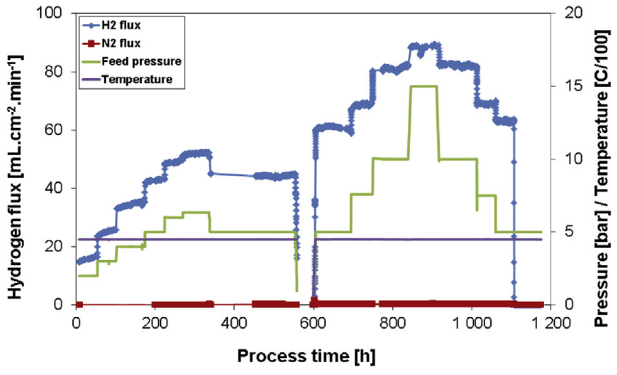

Fig. 2 – H_2 flux during 1100 h up to 15 bars at an operating temperature of 450 °C. Feed applying 60% H_2 in N_2 at 200 $NmLmin^{-1}$, Ar sweep flow rate at 50 $NmLmin^{-1}$. The N_2 leakage flux remained below the detection limit throughout the experiment. Reprinted from Ref. [35] with permission from Elsevier.

Results and discussion

Fig. 3a presents a surface-view SEM image of the $Pd_{77}Ag_{23}$ membrane after operation over 1100 h showing clearly the pattern of the feed channel and fin section of the microchannel-configured module. A high hillock density was present on the feed surface of the gas feed channels, while the phenomenon was residual at the area under the fins (Fig. 3 (b) and (c)). The hillocks are probably a response to stress fields generated by the transmembrane pressure difference and their formation may have been assisted by hydrogen-induced lattice migration [38,39] due to the enhanced concentration of vacancies [40] in the area below the H_2-permeation channels. The variations in hillock size and distribution detected in Fig. 3 (b) reflect the architecture of the porous support on the permeate side [19,35,36,41], with finer hillocks occurring at the contact points with the porous steel support (white dots in Fig. 3 (b) and (d)), which further could imply for a relation between hillock size and local hydrogen flux. The microstructure of the membrane cross section was similar in both areas, *i.e.* under the gas feed channels and under the fin section, frequently consisting of long columnar grains with high density of twins (arrows in Fig. 3 (f) and (g)).

Fig. 4 shows cross-sectional bright-field TEM images and corresponding SAED patterns of the $Pd_{77}Ag_{23}$ film in as-prepared and tested condition. The strong diffraction contrast exhibited by the as-prepared (sputtered) microstructure revealed heavy strain with coherency domains of only tens of nanometers (Fig. 4 (a) and (b)) without a clear preferred crystallographic orientation (see the nearly uniform intensity of the rings in Fig. 4 (c)). Operation at high temperature changed dramatically the sputtered microstructure into heavily twinned columnar grains (Fig. 4 (d) and (e)), resulting into a uniaxial ⟨111⟩ fiber texture normal of the substrate surface (see Fig. 4 (f), although the nearly continuous 111 ring in the powder diffraction pattern attests for the presence of other orientations). The extensive recrystallization into twinned columnar grains is remarkable since a relatively low atomic mobility is expected at 450 °C [42,43]. Therefore, superabundant vacancies, known to be present in Pd under high hydrogen pressures [23], may have contributed to enhance the microstructural transformation. After operation at 450 °C, the $Pd_{77}Ag_{23}$ membrane shows less strain contrast than the previously investigated pure Pd membrane [17], mainly due to the absence of miscibility gap in the Pd-Ag-H system down to room temperature [24]. Nevertheless, residual diffraction contrast in the twin domains (see arrows in Fig. 4 (e)) indicate the presence of dislocation loops. These defects have probably been generated during cooling due to supersaturation of dissolved $H_x\square$ complexes [44] that clustered and collapsed into vacancy disks, with H diffusing out due to the low H_2 partial pressure. Even though it is shown that alloying with Ag decreases the miscibility gap to below room temperature [24], and that fully alloyed Pd-Ag alloy membranes tolerate temperature cycling under H_2 down to 373 K [45], an adequate flushing strategy to fully deplete the Pd-Ag film for hydrogen

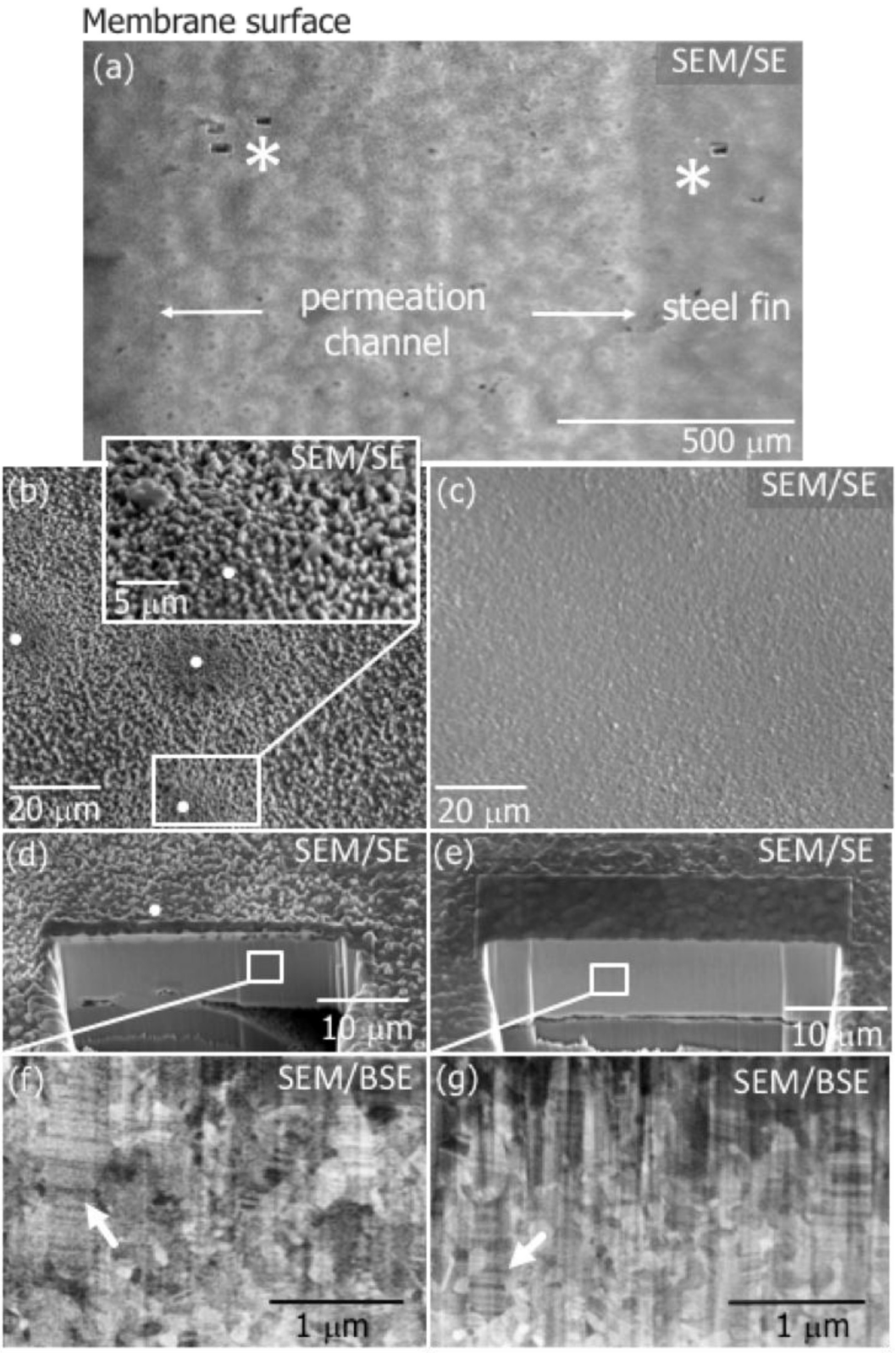

Fig. 3 – SEM images of the tested $Pd_{77}Ag_{23}$ membrane: (a) Feed surface observed at glancing angle. Stars indicate the sites of FIB trenches and extraction of TEM lamellas. Magnified details of (b) feed surface at the permeation channel and (c) under the steel fin. (d) and (e) Cross-sections produced by FIB at, respectively, the permeation channel and under the steel fin. (f) and (g) Grain structure, respectively, at the permeation channel and under the steel fin. The white circles in (b) and (d) indicate positions above contact points with the porous support. The arrows in (f) and (g) indicate twinned columnar grains.

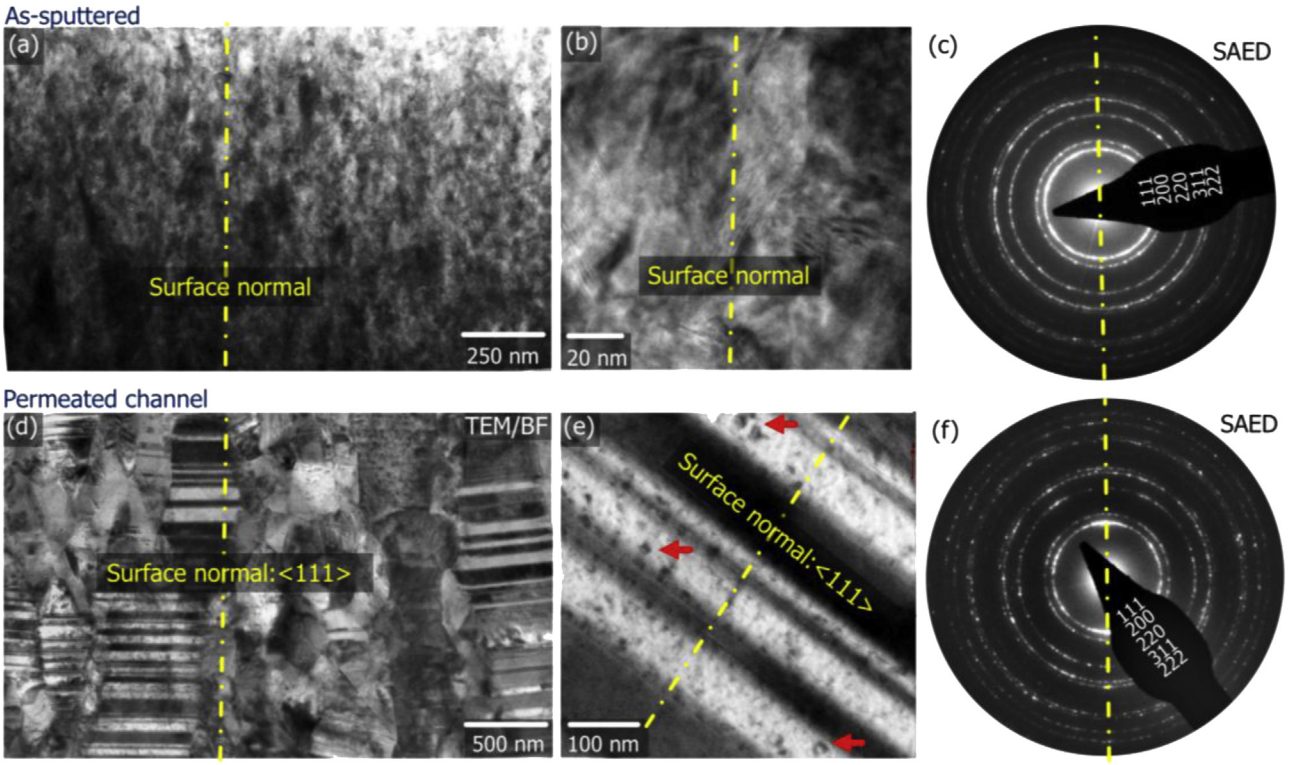

Fig. 4 – Bright-field TEM images of the $Pd_{77}Ag_{23}$ membrane: (a) as-sputtered sample and (e) sample taken from a permeation channel after testing. (b) and (e) are magnified details of, respectively, (a) and (d). (c) and (f) are electron diffraction patterns of, respectively, (b) and (e). The axial yellow lines indicate the normal to the membrane surface. The arrows in (e) point to dislocation loops. (For interpretation of the references to colour in this figure legend, the reader is referred to the Web version of this article.)

prior to cooling is thus required to ascertain membrane stability during multiple shut-down and start-up procedures.

STEM/HAADF observations of the tested membrane revealed a high density of cavities along the columnar GBs, with sizes typically <20 nm (Fig. 5). These observations are consistent with the results obtained previously for pure Pd membranes produced by electroless plating [17] and similar cavities have been reported for Pd [46], Ni [47] and Cu, W and Mo [48,49] exposed to H_2. Due to the typically intense variations in diffraction contrast, these small cavities are not clearly discernible in bright-field TEM images (see Fig. 4 (d)) but are conspicuous when observed under the mass-contrast conditions of HAADF (Fig. 5). The difference in the contrast-generating mechanisms of the two observation modes justifies why the presence of cavities in Pd-based membranes often goes unnoticed in conventional electron microscopy.

As reported for other metals, hydrogen is proposed to be strongly involved in the formation of cavities in Pd-based membranes [17]. While diffusing through the metal lattice, atomic hydrogen is trapped in multiple numbers in metal vacancies, forming $H_x\square$ complexes with high binding energy [44]. As a result, the energy needed for vacancy formation is significantly lowered, which drastically increases the total vacancy concentration [50]. This, in turn, provides additional trapping, increasing the apparent solubility of H by orders of magnitude [51]. In the presence of continuous supply and trapping of H atoms, neighboring vacancies, which normally would strongly repel each other, might aggregate to form multivacancy defects that coalesce into vacancy clusters and subsequently into the observed cavities when the local concentration exceeds the $H_x\square$ solubility limit. These conditions could easily be met at grain boundaries, which work as hydrogen/vacancy sinks and tend to act as preferred nucleation sites for cavities. It should be noted that twin boundaries on (111) planes are not efficient traps/sinks for $H_x\square$ complexes (see Fig. 5 (a) and (b)). These cavities grow by continuous accretion of $H_x\square$ complexes with ejection of the metal atoms initially present at the site into the vacant positions left in the host matrix. Grain boundary segregation of Pd or Ag is not expected to play a role in the cavity formation as EDS was unable to pick up any chemical segregation, with Ag appearing to be in equal solid solution everywhere in the membrane.

In the proposed cavity growing scheme, the metal atoms emerge at the surface due to long-range diffusional fluxes and such mechanism may contribute to hillock formation (see Fig. 3). The trapped hydrogen recombines into molecular form and starts building up pressure inside the cavity forming thus a hydrogen bubble [52]. The internal pressure counteracts the strong effect of the cavity surface energy at these small scales, which would otherwise drive the collapse of the cavity. Palladium presents a considerable average surface free energy ($\bar{\gamma} \approx 2\ J\ m^{-2}$ [53]) and, although adsorption of hydrogen is expected to lower considerably the interfacial energy of the cavities [50], stabilization and growth of such structures is

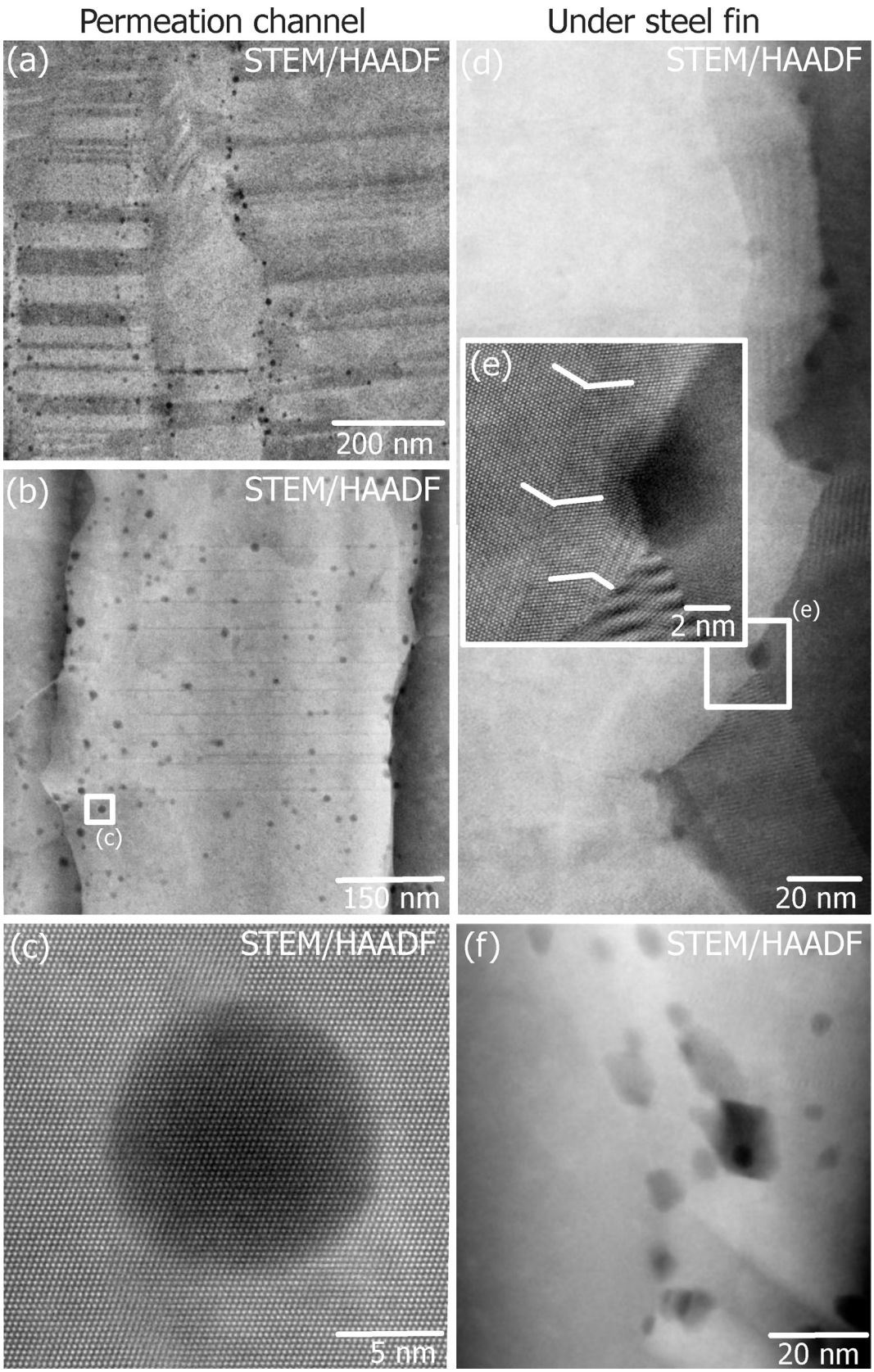

Fig. 5 – (a) Columnar grains at the permeation channel with high density of cavities at the GBs. (b) Region with in-plane grain boundary. (c) Magnified detail of (b). (d) Columnar grains at the blocked region showing lower density of cavities at the GBs. (e) Magnified detail of (d) showing a cavity at a grain boundary. Nearby coherent twin boundaries are indicated. (f) Non-spherical cavities in a region blocked to H_2 permeation under a steel fin. Convergence angle of 22 mrad and collection angle of 75–200 mrad in all images.

likely to require relatively high internal pressure [54,55]. Indeed, under conditions of high mobility of the lattice atoms, unless an effective counteracting internal H_2 pressure exists, the excess energy associated with the spherical surface would promptly function as vacancy source recruiting lattice atoms to fill the empty space, closing up the cavity.

As mentioned before, no striking differences have been detected between the grain structure in the permeation channels (Fig. 3 (f)) and the grain structure in the regions blocked by the steel fins (Fig. 3 (g)). However, the density of cavities was noticeably higher at the columnar GBs across the permeation channel (Fig. 5 (a) and (b)) than in the blocked regions (Fig. 5 (d) and (e)). This indicates an important effect of active H_2 permeation on the development of such cavities, justified by the local gradients in pressure and hydrogen concentration as schematically depicted in Fig. 1. Furthermore, while the cavities were nearly spherical in the permeation channels (Fig. 5 (a) to (c)), the cavities tended to be irregularly shaped in the regions under the fins (Fig. 5 (d) to (f)). The spherical shapes confirms the hypothesis of a significant internal pressure, whereas the irregularly shaped cavities indicate a lower internal pressure in the regions blocked for H_2 permeation. A quantitative analysis of the strain around such small bubbles (<20 nm) from STEM images is troublesome, even for very thin TEM samples, since any local change in the projected position of the atomic columns around the bubble is diluted by the layers of perfect crystal above and below the bubble. Nevertheless, bubbles presenting weak lattice periodicities in their (projected) internal regions, *i.e.* with relatively low proportion of embedding crystal above and below, were investigated by Fourier filtering and geometric phase analysis (GPA). Fig. 6 shows an example of such analysis for a nearly spherical bubble (Fig. 6 (a)) with the lattice columns appearing undistorted in the Bragg filtered image (Fig. 6 (b)) and only residual strain being detected by GPA (Fig. 6 (c) and (d)). At the time of the analysis, any hydrogen initially present in the bubble is expected to have diffused out of the TEM lamella, while the cavity was preserved due to the low lattice mobility at room temperature. Nevertheless, the spherical shape and the residual distortion of the lattice planes around these 3-D defects suggest that near equilibrium conditions existed during the

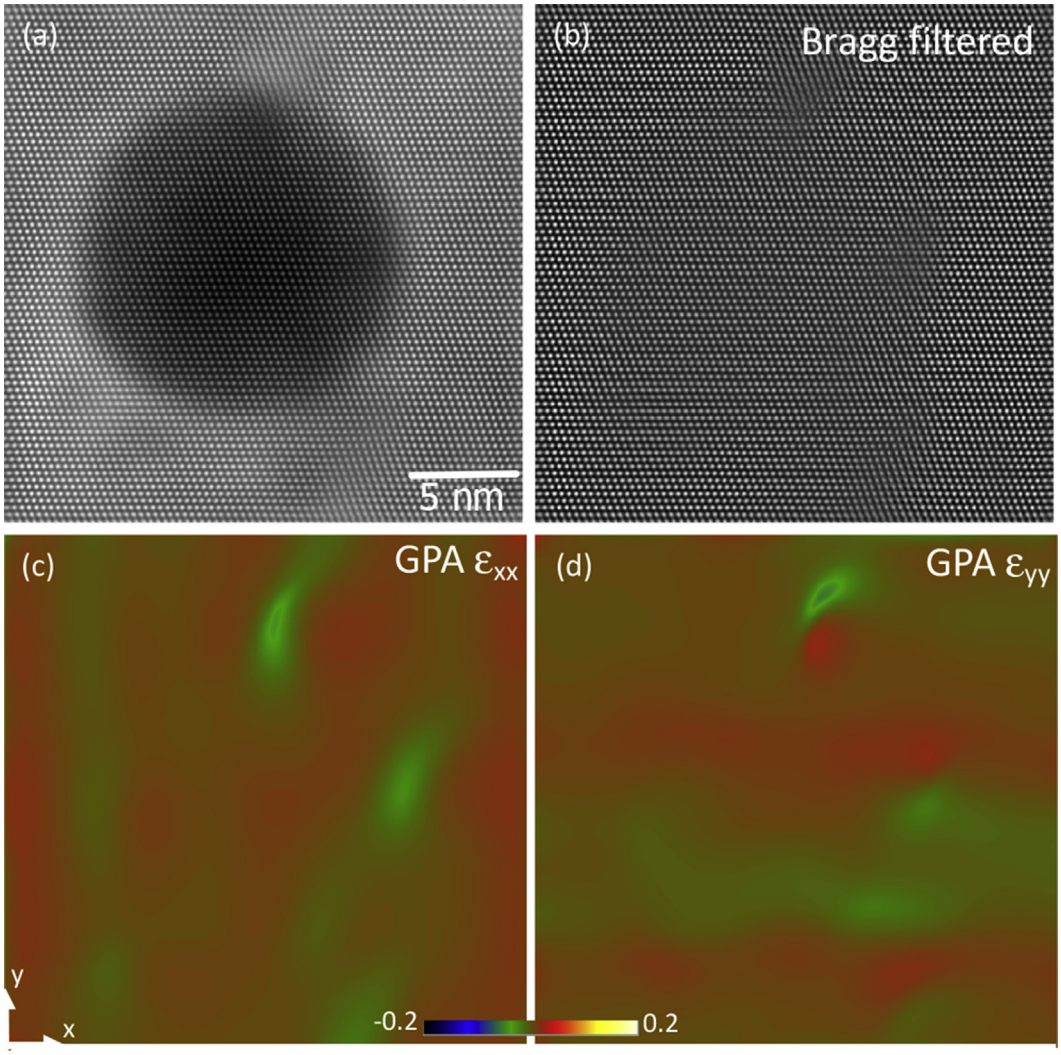

Fig. 6 – Analysis of strain around the hydrogen bubble shown in Fig. 5 (c): (a) low-pass Fourier filtered, (b) only Bragg reflections allowed in the inverse Fourier transform, (c), ε_{xx} strain map (d), ε_{yy} strain map.

formation of the bubble, confirming thus the presence of a high internal pressure.

We have shown that magnetron-sputtered Pd-Ag membranes are afflicted by H_2 bubble formation, which is similar to our previous report on the pure Pd membrane prepared by electroless plating [17]. The fabrication technique might, however, affect the resulting bubble density through the inherently different microstructural characteristics, but an evaluation of these effects will require more systematic investigation. In addition, membrane parameters like alloy composition, thickness and support material need to be similar if targeting a rigorous comparison of manufacturing technique. This has not been done in the current study. The observed bubbles did not result in significant leakage in the conditions studied [18], but long exposure to H_2 at high temperature can lead to percolation of bubbles into channels likely to correspond to the initial stages of pinholes, as discussed previously [17]. Although simulations and additional experiments are required for a quantitative description of the atomic mechanisms proposed above, the qualitative discussion enables to point directions for enhancement of membrane stability. Some form of systematic annealing at high temperatures in the absence of hydrogen to close up existing cavities is proposed as healing procedure after normal operation. In addition, since Ag eliminates the miscibility gap at the operation conditions [24], Pd-Ag alloy membranes can tolerate temperature cycling in H_2 atmospheres down to 373 K without formation of extensive dislocation networks [45], which acts as a mitigation measure for cavity nucleation. However, adequate flushing to fully deplete the Pd-Ag film from hydrogen trapped in $H_x\square$ complexes is necessary prior to cooling to room temperature to avoid defects such as dislocation loops that may act as nuclei for cavities in subsequent cycles.

Conclusions

Cavities filled with molecular hydrogen, *i.e.* H_2 bubbles, form during high-temperature operation at high-angle grain boundaries as a result of local supersaturation. The present results show that the presence of Ag does not prevent the formation of the fore-mentioned bubbles, although a quantitative measure of the alloying effect requires additional experiments. Nonetheless, the presence of Ag prevents the formation of dislocations when H-saturated Pd is cycled through the miscibility gap, and this precludes the nucleation of cavities at dislocation networks, which has been observed in pure palladium membranes. We have shown that both electroless plating and magnetron-sputtered Pd-based membranes are afflicted by cavity formation. However, the fabrication technique may affect the resulting density through the inherently different microstructural characteristics, but an evaluation of these effects will require more systematic investigation.

Acknowledgements

The support from European Union and the Research Council of Norway (RCN) through the RCN-CLIMIT (Project Numbers: 215666 and 281824) program, and the FCH JU AutoRE project (Contract no.: 671396) are gratefully acknowledged. The authors also acknowledge the Norwegian Centre for Transmission Electron Microscopy, NORTEM.

REFERENCES

[1] Energy roadmap 2050 - European commission - COM(2011) 885. 2011.
[2] Materials roadmap enabling low carbon technologies - European commission - SEC(2011) 1609. 2011.
[3] Peters TA, Bredesen R, Venvik HJ. Pd-based membranes in hydrogen production: long-term stability and contaminant effects membrane engineering for the treatment of gases: volume 2: gas-separation issues combined with membrane reactors (2). The Royal Society of Chemistry; 2018. p. 177–211.
[4] Oertel M, Schmitz J, Weirich W, Jendryssek-Neumann D, Schulten R. Steam reforming of natural gas with intergrated hydrogen separation for hydrogen production. Chem Eng Technol 1987;10:248–55.
[5] Uemiya S. State-of-the-Art of supported metal membranes for gas separation. Separ Purif Rev 1999;28:51–85.
[6] Lin YM, Rei MH. Process development for generating high purity hydrogen by using supported palladium membrane reactor as steam reformer. Int J Hydrog Energy 2000;25:211–9.
[7] Roses L, Manzolini G, Campanari S, De Wit E, Walter M. Techno-economic assessment of membrane reactor technologies for pure hydrogen production for fuel cell vehicle fleets. Energy Fuels 2013;27:4423–31.
[8] Abdollahi M, Yu J, Liu PKT, Ciora R, Sahimi M, Tsotsis TT. Ultra-pure hydrogen production from reformate mixtures using a palladium membrane reactor system. J Membr Sci 2012;390–391:32–42.
[9] Loreti G, Facci AL, Peters T, Ubertini S. Numerical modeling of an automotive derivative polymer electrolyte membrane fuel cell cogeneration system with selective membranes. Int J Hydrog Energy 2019;44:4508–23.
[10] Kurokawa H, Yakabe H, Yasuda I, Peters T, Bredesen R. Inhibition effect of CO on hydrogen permeability of Pd–Ag membrane applied in a microchannel module configuration. Int J Hydrog Energy 2014;39:17201–9.
[11] Yakabe H, Kurokawa H, Shirasaki Y, Yasuda I. Operation of a palladium membrane reformer system for hydrogen production: the case of tokyo gas palladium membrane technology for hydrogen production, carbon capture and other applications. Woodhead Publishing; 2015. p. 303–18.
[12] Shirasaki Y, Tsuneki T, Ota Y, Yasuda I, Tachibana S, Nakajima H, Kobayashi K. Development of membrane reformer system for highly efficient hydrogen production from natural gas. Int J Hydrog Energy 2009;34:4482–7.
[13] Basile A. Hydrogen production using Pd-based membrane reactors for fuel cells. Top Catal 2008;51:107–22.
[14] Gallucci Fausto F, van Sint Annaland Martin, editors. Process Intensification for Sustainable Energy Conversion. John Wiley & Sons, Ltd; 2015.
[15] Bredesen R, Jordal K, Bolland A. High-temperature membranes in power generation with CO_2 capture. Chem Eng Process 2004;43:1129–58.
[16] Guazzone F, Ma YH. Leak growth mechanism in composite Pd membranes prepared by the electroless deposition method. AIChE J 2008;54:487–94.
[17] Peters TA, Carvalho PA, van Wees JF, Overbeek JP, Sagvolden E, van Berkel FPF, Løvvik OM, Bredesen R. Leakage

evolution and atomic-scale changes in Pd-based membranes induced by long-term hydrogen permeation. J Membr Sci 2018;563:398–404.
[18] Castro-Dominguez B, Ma LC, Mardilovich IP, Kazantzis NK, Ma YH. Integrated experimental-technoeconomic analysis of the lifetime of Pd–Au membranes. Ind Eng Chem Res 2016;55:10160–71.
[19] Peters TA, Tucho WM, Ramachandran A, Stange M, Walmsley JC, Holmestad R, Borg A, Bredesen R. Thin Pd-23% Ag/stainless steel composite membranes: long-term stability, life-time estimation and post-process characterisation. J Membr Sci 2009;326:572–81.
[20] Humphreys FJ, Hatherly M. The structure and energy of grain boundaries. In: Humphreys FJ, Hatherly M, editors. Recrystallization and related annealing phenomena. 2nd ed. Oxford: Elsevier; 2004. p. 91–119.
[21] Goldman S. Generalizations of the Young-Laplace equation for the pressure of a mechanically stable gas bubble in a soft elastic material. J Chem Phys 2009;131:184502.
[22] Conde JJ, Marono M, Sanchez-Valdes S. Pd-based membranes for hydrogen separation: review of alloying elements and their influence on membrane properties. Separ Purif Rev 2017;46:152–77.
[23] Holleck GL. Diffusion and solubility of hydrogen in palladium and palladium-silver alloys. J Phys Chem 1970;74:503–11.
[24] Grashoff GJ, Pilkington CE, Corti CW. Purification of hydrogen. Platin Met Rev 1983;27:157–69.
[25] Uemiya S, Matsuda T, Kikuchi E. Hydrogen permeable palladium-silver alloy membrane supported on porous ceramics. J Membr Sci 1991;56:315–25.
[26] Sakamoto Y, Hirata S, Nishikawa H. Diffusivity and solubility of hydrogen in Pd-Ag and Pd-Au alloys. J Less Common Met 1982;88:387–95.
[27] D.L.McKinley, US Patent 3,439,474, 22-4-1969.
[28] D.L.McKinley, US Patent 3,350,845, 7-11-1967.
[29] McCool B, Xomeritakis G, Lin YS. Composition control and hydrogen permeation characteristics of sputter deposited palladium-silver membranes. J Membr Sci 1999;161:67–76.
[30] Witjens LC, Bitter JH, van Dillen AJ, Arnoldbik WM, Habraken FHPM, de Jong KP. Improving the control of the electroless plating synthesis of Pd/Ag membranes for hydrogen separation using Rutherford backscattering. J Membr Sci 2005;254:241–8.
[31] Gade SK, DeVoss SJ, Coulter KE, Paglieri SN, Alptekin GkO, Way JD. Palladium-gold membranes in mixed gas streams with hydrogen sulfide: effect of alloy content and fabrication technique. J Membr Sci 2011;378:35–41.
[32] Kulprathipanja A, Alptekin GO, Falconer JL, Way JD. Pd and Pd-Cu membranes: inhibition of H_2 permeation by H_2S. J Membr Sci 2005;254:49–62.
[33] Peters TA, Stange M, Veenstra P, Nijmeijer A, Bredesen R. The performance of Pd-Ag alloy membrane films under exposure to trace amounts of H_2S. J Membr Sci 2016;499:105–15.
[34] Peters TA, Polfus JM, Stange M, Veenstra P, Nijmeijer A, Bredesen R. H_2 flux inhibition and stability of Pd-Ag membranes under exposure to trace amounts of NH_3. J Membr Sci 2016;152:259–65.
[35] Peters TA, Stange M, Sunding MF, Bredesen R. Stability investigation of micro-configured Pd–Ag membrane modules – Effect of operating temperature and pressure. Int J Hydrogen Energy 2015;40:3497–505.
[36] Peters TA, Stange M, Bredesen R. On the high pressure performance of thin supported Pd-23%Ag membranes - evidence of ultrahigh hydrogen flux after air treatment. J Membr Sci 2011;378:28–34.
[37] Koch CT. FRWRtools plugin. 2006.
[38] Flanagan TB, Clewley JD, Noh H, Barker J, Sakamoto Y. Hydrogen-induced lattice migration in Pd–Pt alloys. Acta Mater 1998;46:2173–83.
[39] Flanagan TB, Noh H. A possible role for hydrogen-induced lattice migration in alloy materials processing. J Alloy Comp 1995;231:1–9.
[40] Fukai Y, Akuma N. Formation of superabundant vacancies in Pd hydride under high hydrogen pressures. Phys Rev Lett 1994;73:1640–3.
[41] Peters TA, Stange M, Klette H, Bredesen R. High pressure performance of thin Pd-23%Ag/stainless steel composite membranes in water gas shift gas mixtures; influence of dilution, mass transfer and surface effects on the hydrogen flux. J Membr Sci 2008;316:119–27.
[42] Rowland RL, Nachtrieb NH. Self-diffusion of palladium in silver-palladium alloys. J Phys Chem 1963;67:2817–21.
[43] Peterson NL. Isotope effect in self-diffusion in palladium. Phys Rev 1964;136:A568–74.
[44] Fukai Y. Formation of superabundant vacancies in metal hydrides at high temperatures. J Alloy Comp 1995;231:35–40.
[45] Zeng G, Goldbach A, Shi L, Xu H. On alloying and low-temperature stability of thin, supported PdAg membranes. Int J Hydrogen Energy 2012;37:6012–9.
[46] Miraglia S, Fruchart D, Hlil EK, Tavares SSM, Dos Santos D. Investigation of the vacancy-ordered phases in the Pd-H system. J Alloy Comp 2001;317–318:77–82.
[47] Osono H, Kino T, Kurokawa Y, Fukai Y. Agglomeration of hydrogen-induced vacancies in nickel. J Alloy Comp 1995;231:41–5.
[48] Nunes D, Carvalho PA, Mateus R, Nogueira ID, De Deus AM, Correia JB, Shohoji N, Gomes RB, Femandes H, Silva C, Franco N, Alves E. In: Materials Research society symposium proceedings; 2009. p. 29–34.
[49] Nunes D, Mateus R, Nogueira ID, Carvalho PA, Correia JB, Shohoji N, Gomes RB, Fernandes H, Silva C, Franco N, Alves E. Microstructural evolution in tungsten and copper probes under hydrogen irradiation at ISTTOK. J Nucl Mater 2009;390–391:1039–42.
[50] Nazarov R, Hickel T, Neugebauer J. Ab initio study of H-vacancy interactions in fcc metals: implications for the formation of superabundant vacancies. Phys Rev B 2014;89.
[51] Lu G, Kaxiras E. Hydrogen embrittlement of aluminum: the crucial role of vacancies. Phys Rev Lett 2005;94, 155501.
[52] Geng WT, Wan L, Du JP, Ishii A, Ishikawa N, Kimizuka H, Ogata S. Hydrogen bubble nucleation in alpha-iron. Scripta Mater 2017;134:105–9.
[53] Tran R, Xu Z, Radhakrishnan B, Winston D, Sun W, Persson KA, Ong SP. Surface energies of elemental crystals. Scientific Data 2016;3:160080.
[54] Liu H, Cao G. Effectiveness of the Young-Laplace equation at nanoscale. Nature Sci Rep 2016;6, 23936.
[55] Caro A, Schwen D, Hetherly J, Martinez E. The capillarity equation at the nanoscale: gas bubbles in metals. Acta Mater 2015;89:14–21.